



## Role of metal-N-C electron transport channel within g-C<sub>3</sub>N<sub>4</sub> for promoting water purification of photocatalytic ozonation

Yushan Tan <sup>a,1</sup>, Weirui Chen <sup>b,1,\*</sup>, Gaozu Liao <sup>a</sup>, Xukai Li <sup>a</sup>, Jing Wang <sup>a</sup>, Jianbing Wang <sup>c,\*</sup>, Yiming Tang <sup>a</sup>, Laisheng Li <sup>a,\*</sup>

<sup>a</sup> School of Environment, South China Normal University, Key Laboratory of Theoretical Chemistry of Environment, Ministry of Education, Guangdong Provincial Engineering Technology Research Center for Drinking Water Safety, Guangdong Provincial Key Lab of Functional Materials for Environmental Protection, Guangzhou 510006, China

<sup>b</sup> School of Environmental Science and Engineering, Guangdong University of Technology, Guangzhou 510006, China

<sup>c</sup> School of Chemical and Environmental Engineering, China University of Mining and Technology (Beijing), Beijing 100083, PR China



### ARTICLE INFO

#### Keywords:

Photocatalytic ozonation  
Single-atom catalysts  
Metal-N-C  
Electron transport channel  
Hydroxyl radical

### ABSTRACT

The sluggish  $Me^{(n+m)+}/Me^{n+}$  cycle of metal based catalysts set an obstacle for catalytic ozonation, which not only restrained O<sub>3</sub> activation efficiency but also damaged their poor stability. Herein, series of atomic metal-doped g-C<sub>3</sub>N<sub>4</sub> with Me-N-C electron transport channels and the photocatalytic ozonation process (PCO) were designed to refresh metal active sites by photo-electron ( $e_{cb}$ ) and overcome the basic need of sacrificing catalysts' inherent electron to activate O<sub>3</sub> into •OH. Experimental and DFT results demonstrated that, oxalic acid degradation in PCO was metal-dependent and followed the trends: Fe-CN (98.5%, 0.228 min<sup>-1</sup>)>Mn-CN (98.9%, 0.154 min<sup>-1</sup>)>Co-CN (93.7%, 0.097 min<sup>-1</sup>). Two distinct •OH generation pathways were proposed. Fe-N-C and Co-N-C were capable of utilizing  $e_{cb}$  to boost metal redox cycle and they activated O<sub>3</sub> by  $e_{cb}$ . But Mn-N-C failed to realize such redox cycle and activated O<sub>3</sub> with Mn center sacrificing its inherent electron. This study was useful for designing catalysts for PCO.

### 1. Introduction

The intensification of urbanization and industrialization posed a great threat to water security and called for the greater efficiency of water treatment process. Advanced oxidation processes (AOPs) were popular techniques in decontamination [1,2]. Among the employed AOPs, heterogeneous catalytic ozonation (HCO) was the most promising one, which was featured for its high mineralization rate and low toxic by-products accumulation [3–5]. Metal-based materials were the mainstream catalysts in HCO and the interfacial electron migration induced by metal redox cycle was vital for ozone (O<sub>3</sub>) activation [6,7]. Under the drive of exogenous electron, O<sub>3</sub> was conveyed into various reactive oxygen species (ROS) like hydroxyl radical (•OH), superoxide radical (•O<sub>2</sub><sup>−</sup>), etc [8]. However, such activation way required the continuous sacrifice of inherent electrons of metal species, which resulted in the accumulation of oxidized metal (considered less active) in catalysts [9]. The sluggish  $Me^{(n+m)+}/Me^{n+}$  redox cycle not only restrained the interfacial electron migration rate but also resulted in the

poor activity and stability of catalysts [10,11].

To this end, various strategies had been put forward to accelerate the redox cycle. Bimetallic catalysts was designed to accelerate the interfacial electron transfer via the help of bimetal interaction [12]. The guest metal could accelerate the metal redox cycle by contributing its inherent electrons to refresh the host metal from  $Me^{(n+m)+}$  to  $Me^{n+}$  [13, 14]. Yu et al. had found that the two redox couples (Fe<sup>3+</sup>/Fe<sup>2+</sup> and Co<sup>2+</sup>/Co<sup>3+</sup>) in Fe-Co/ZrO<sub>2</sub> bimetallic catalysts enhanced the interfacial electron transfer and resulted in the higher O<sub>3</sub> activation efficiency [15]. But the overall electron behavior between catalysts and O<sub>3</sub> remained the same as the conventional one. Recently, researchers had verified the feasibility of combining photocatalysis (PC) with HCO (named photocatalytic ozonation, PCO). The fundamental basis of PCO process was to activate O<sub>3</sub> via photogenerated-electron ( $e_{cb}$ ) [16]. Xiao et al. suggested that O<sub>3</sub> could act as an electron acceptor to capture the  $e_{cb}$  produced by photocatalysts under visible light irradiation, generating strongly oxidative radicals such as •OH to degrade oxalic acid [17]. Our previous study investigated the catalytic activity of halogen-doped g-C<sub>3</sub>N<sub>4</sub> (CN) in

\* Corresponding authors.

E-mail addresses: [wr\\_chen@gdut.edu.cn](mailto:wr_chen@gdut.edu.cn) (W. Chen), [wangjb@cumtb.edu.cn](mailto:wangjb@cumtb.edu.cn) (J. Wang), [llsh@scnu.edu.cn](mailto:llsh@scnu.edu.cn) (L. Li).

<sup>1</sup> Authors contributed equally to this work

PCO process and discovered that the halogen doping led to a non-uniform distribution of electrons on CN and the formation of hydrophobic sites, which favored the  $O_3/O_2$  mass transfer and the  $O_3$  activation capacity [18]. Though these nonmetal catalysts successfully activated  $O_3$  into  $\bullet OH$  via a single-electron reduction (SER) process (Eq. (1)), the mismatch of  $e_{cb}$  excitation rate and  $O_3$  mass transfer rate restrained the efficiency of PCO. Moreover, non-metallic elements with high electronegativity were unfavorable for the escape of  $e_{cb}$  compared to metallic species. A great deal of  $e_{cb}$  remained invalid and quickly recombined with photogenerated-hole ( $h_{vb}^+$ ) or consumed by  $O_2$  via the inefficient three-electron reduction (TER) pathway (Eq.(2)).



To further improve the utilization rate of  $e_{cb}$  and  $O_3$ , herein, we synthesized a series of atomic metal doped g-C<sub>3</sub>N<sub>4</sub> (named Me-CN, Me= Fe, Mn, and Co). The active metal was atomically anchored by N atom within s-triazine ring to conduct Me-N-C electron channel, which was designed to store and convert  $e_{cb}$  for the further  $O_3$  activation. Oxalic acid (OA), a high refractory compound, was selected as a main target pollutant to evaluate the catalytic activity. Our results suggested that OA removals was in the order of Fe-CN (98.5%,  $k=0.228\text{ min}^{-1}$ ) > Mn-CN (98.9%,  $k=0.154\text{ min}^{-1}$ ) > Co-CN (93.7%,  $k=0.097\text{ min}^{-1}$ ). The catalytic activities of Me-CN were associated with the affinity of metal center towards  $e_{cb}$ . Me-N-C unit within Fe-CN and Co-CN could serve as “ $e_{cb}$  depot”. The captured  $e_{cb}$  was then used to realize the metal redox cycle and finally participated in  $O_3$  activation. Though Mn-CN also exhibited a high PCO activity, it failed to utilize  $e_{cb}$  to reduce the oxidized Mn, resulting in its poor stability. Comparative PCO experiments, characterizations, and DFT calculations were employed to reveal the metal-dependent mechanism.

## 2. Experimental sections

### 2.1. Synthesis of Me-CN and CN

Typically, 1 g dicyandiamide and 0.5 mmol metal salts ( $FeCl_3 \cdot 6H_2O$ ,  $Co(oAc)_2 \cdot 4H_2O$ , and  $MnCl_2$ ) were added into deionized water (20 mL) according to the reported literatures [19–22]. To synthesize the Fe-CN, Co-CN, and Mn-CN catalysts, a mixed solution of dicyandiamide and metal salts was prepared and then placed in a water bath under stirring at 60 °C for 1 h. Next, the temperature was gradually increased to 90 °C to evaporate all the water. The remaining mixture was then dried and ground into a fine powder before being heated to 600 °C for 3 h at a rate of 10 °C/min in a  $N_2$  atmosphere to obtain Fe-CN, Co-CN, and Mn-CN. The g-C<sub>3</sub>N<sub>4</sub> (CN) was obtained via a similar process without the addition of metal ions.

### 2.2. Catalytic performance of Me-CN in PCO

The photocatalytic ozonation (PCO) was carried out at 25 °C in a double glass column. 1 L solution with 10 mg/L of oxalic acid (OA) and 0.1 g/L of catalyst was mixed. Dry air was directly used to produce ozone ( $O_3$ ), which was then continuously aerated into the reactor from the button aeration plate. The flow rate of was 1.0 L/min and  $O_3$  input was 20 mg/h. A 300 W long arc xenon lamp obtained from Guangzhou Xingchuang Electronics Co., Ltd was used to simulate sunlight. The real intensity of light was determined as  $\sim 310\text{ W/m}^2$ . The reaction device could be found in Fig.S1. All water samples were filtered by 0.45 μm organic filter and quenched by  $Na_2S_2O_3$  before analysis. OA concentration was analyzed by high-performance liquid chromatography (HPLC, LC10A, Shimadzu, Japan) equipped with a C18 column (4.6 mm×150 mm), the injection volume was 100 μL and the determined wavelength was 210 nm. The mobile phase was ultrapure water added with proper amount of phosphoric acid (pH=2.5). The reaction

rates were estimated by the pseudo-first-order equation (Eq.(3)), and the synergy factor ( $\eta$ ) was estimated by the Eq.(4). Average quantum efficiencies (AQEs) could be obtained via Eq.(5).

$$Ln(C_0/C_t) = k * t \quad (3)$$

$$\eta = K_{PCO} / (K_p + K_{HCO}) \quad (4)$$

$$AQEs = \frac{N_e}{N_p} * 100\% = \frac{10^9 * (v * N_A * K) * (h * c)}{(I * A * \lambda)} * 100\% \quad (5)$$

where  $C_0$  was the concentration of the initial contaminant,  $C_t$  was the concentration of the contaminant at a reaction time,  $k$  was the first-order kinetic rate,  $t$  was the reactive time, and  $\eta$  represented the synergy factor of light irradiation (P) and heterogeneous catalytic ozonation (HCO) in the PCO process.  $N_e$  was the total number of transferred electrons,  $N_p$  was the number of incident photons,  $v$  was the reaction rate (mol/s),  $N_A$  was  $6.02 \times 10^{23}\text{ mol}^{-1}$ ,  $K$  was the number of transferred electron,  $h$  was planck constant,  $6.62 \times 10^{-34}\text{ J*s}$ ,  $c$  was light speed,  $3.0 \times 10^8\text{ m/s}$ ,  $I$  was the optical power density ( $\text{W/m}^2$ ),  $A$  was the incident light area, and  $\lambda$  was the wavelength (nm).

### 2.3. Material characterization

The crystal phases of the CN and Me-CN materials were identified by an X-ray diffraction (XRD, BRUKER D8 ADVANCE) with Cu K $\alpha$  radiation. The Fourier transform infrared (FTIR) spectra were recorded using a Thermo Scientific iN10 (USA). The microstructure of the catalysts was analyzed by high-angle annular dark field scanning tunneling electron microscopy (HAADF-STEM), with STEM mapping using a JEM-ARM300F. The mass fractions of different metals on the catalysts were determined by inductively coupled plasma-atomic emission spectrometry (ICP-MS, Agilent 7700 s (MS), USA). X-ray photoelectron spectroscopy (XPS, Thermo Scientific K-Alpha, USA) was used to investigate the surface chemical properties. X-ray absorption spectroscopy (XAS) was used to obtain the precise coordination structure of Me-CN. The fitting of the extended X-ray absorption fine structure (EXAFS) was carried out by the software Athena and Artemis. Wavelet transform (WT) was applied using the software package developed by Funke and Chukalina using wavelet with  $K=10$ ,  $\sigma=1$ . Py-IR was for the detection of the Lewis acid site of the catalysts on a Thermo fisher Nicolet iS50. The ultraviolet-visible diffuse reflectance spectroscopy (UV-vis DRS, UV-3600, Shimadzu) and photoluminescence spectra (PL, F-4600, Hitachi) were conducted to evaluate the optical properties. Electrochemical and Mott-Schottky measurements were carried out by an electrochemical system (CHI 660E, Chenhua, China). RRED on CHI700E series dual potentiostat (Shanghai Chenhua Instrument Co., Ltd) was used to record the electron transfer number ( $n$ ) of catalysts according to Eq.(6). Collection efficiency was 0.37. Area of glassy carbon disk/ platinum ring was 0.2475 and 0.1866  $\text{cm}^2$ . 0.1 M KOH was used as electrolyte. A scanning range of  $-1.0\text{--}0.2\text{ V}$  (vs. Ag/AgCl) with the speed of 10 mV/s and rotating speed of 1600 rpm was employed.

$$n = 4 \times \frac{I_D}{I_D + I_r/N} \quad (6)$$

Where  $I_D$  was the current density of glassy carbon disk,  $I_r$  was the current density of platinum ring,  $N$  was the collection efficiency.

Electron paramagnetic resonance (EPR, Bruker A300) was used to detect ROS produced during the catalytic reactions.  $\bullet OH$  was recorded in pure water and  $\bullet O_2$  was measured with the coexistence of methanol to reduce the interference of hydroxyl radicals. Detailed instrument parameters were: Injection volume: 10  $\mu\text{L}$ ; Central magnetic field: 3500 G; Sweeping field width: 100 G; Sweeping field time: 30 s; Microwave power: 20.0 mW; Modulation amplitude: 1.0 G.

## 2.4. Method of $R_{CT}$ determination

The  $R_{CT}$  value was defined as the ratio of exposed  $\bullet\text{OH}$  to  $\text{O}_3$  in the solution during the reaction. Larger  $R_{CT}$  values indicated greater  $\bullet\text{OH}$  exposure, which could be expressed by Eq.(7). By establishing a kinetic model to determine the  $R_{CT}$  value, the contribution value of  $\bullet\text{OH}$  in the process of PCO degradation of OA was further explored. When p-CBA was used as the  $\bullet\text{OH}$  indicator, the kinetic equation could be expressed as Eq.(8).

$$R_{CT} = C_{\bullet\text{OH}} / C_{\text{O}_3} \quad (7)$$

$$\ln \frac{C_{\text{p-CBA},t}}{C_{\text{p-CBA},0}} = -k_{\bullet\text{OH}/\text{p-CBA}} * R_{CT} * \int_0^t C_{\text{O}_3,t} dt \quad (8)$$

Where  $C_{\text{p-CBA},0}$  was initial concentration of p-CBA,  $C_{\text{p-CBA},t}$  was the concentration of p-CBA at a reaction time,  $k_{\bullet\text{OH}/\text{p-CBA}}$  was secondary rate constant between  $\bullet\text{OH}$  and p-CBA ( $5 \times 10^9 \text{ M}^{-1}\text{s}^{-1}$ ),  $C_{\text{O}_3,t}$  was the concentration of  $\text{O}_3$  in solution at a certain time.

$\text{O}_3$  concentration could be expressed by Eq.(9). In multiphase reactions, the fate of  $\text{O}_3$  generated from the  $\text{O}_3$  generator included its presence in the aqueous solution and its consumption by the catalyst. Since the initial concentration of  $\text{O}_3$  was the same in both the PCO/CN and PCO/Me-CN systems, it was possible to determine the quantity of  $\text{O}_3$  consumed by the catalyst by measuring the concentration of  $\text{O}_3$  in the aqueous solution.

$$\left( \frac{dC_{\text{O}_3}}{dt} \right)_{\text{CN}} = K_L \alpha * \left( C_{\text{O}_3}^* - C_{\text{O}_3,t} \right) - K_{\text{CN}/\text{O}_3} * C_{\text{CN}} * C_{\text{O}_3,t} \quad (9)$$

Where  $k_L \alpha$  was the volume mass transfer coefficient,  $C_{\text{O}_3}^*$  was the  $\text{O}_3$

saturation concentration in the absence of a solid catalyst,  $k_{\text{CN}/\text{O}_3}$  was the reaction rate constant of CN and  $\text{O}_3$ ,  $C_{\text{CN}}$  was the catalyst concentration.

Eq.(7) was integrated to get Eq.(10). By performing a nonlinear regression analysis of  $C_{\text{O}_3,t}$  with time, the values of a, b, and c in Eq.(10) could be obtained. Finally, by substituting Eq.(8) into Eq.(3), the  $R_{CT}$  value could be found.

$$C_{\text{O}_3,t} = a - b * e^{C*t} \quad (10)$$

Where a was  $(\frac{k_L \alpha * C_{\text{O}_3}}{k_L \alpha + k_{\text{CN}/\text{O}_3}})$ ,  $b * e^{C*t}$  was  $(\frac{e^{-(k_L \alpha * k_{\text{CN}/\text{O}_3})}}{k_L \alpha + k_{\text{CN}/\text{O}_3}})$ .

## 2.5. Quantum chemical calculations

All calculations were conducted by using the Vienna Ab-initio Simulation Package (VASP). The exchange-correlation energies were treated with the spin-polarized generalized gradient approximation and Perdew-Bruke-Ernzerher of functional [23]. A 400 eV plane wave cutoff energy and a  $2 \times 2 \times 1$  k-point sampling were used for all calculations. All crystal structures were optimized with an energy convergence threshold of  $1.0 \times 10^{-5}$  eV and force convergence threshold of 0.03 eV/Å. To avoid interaction between two adjacent surfaces, the vacuum spacing was set as 15.0 Å. Considering the function of Vander Waals force, DFT-D3 method was employed for dispersion correction. The transition state was found by the climbing-image nudged elastic band (CI-NEB) methods. The reasonable transition state was judged based on the vibration direction with only one imaginary frequency. VESTA and vaspkit were used for visualization [24,25].

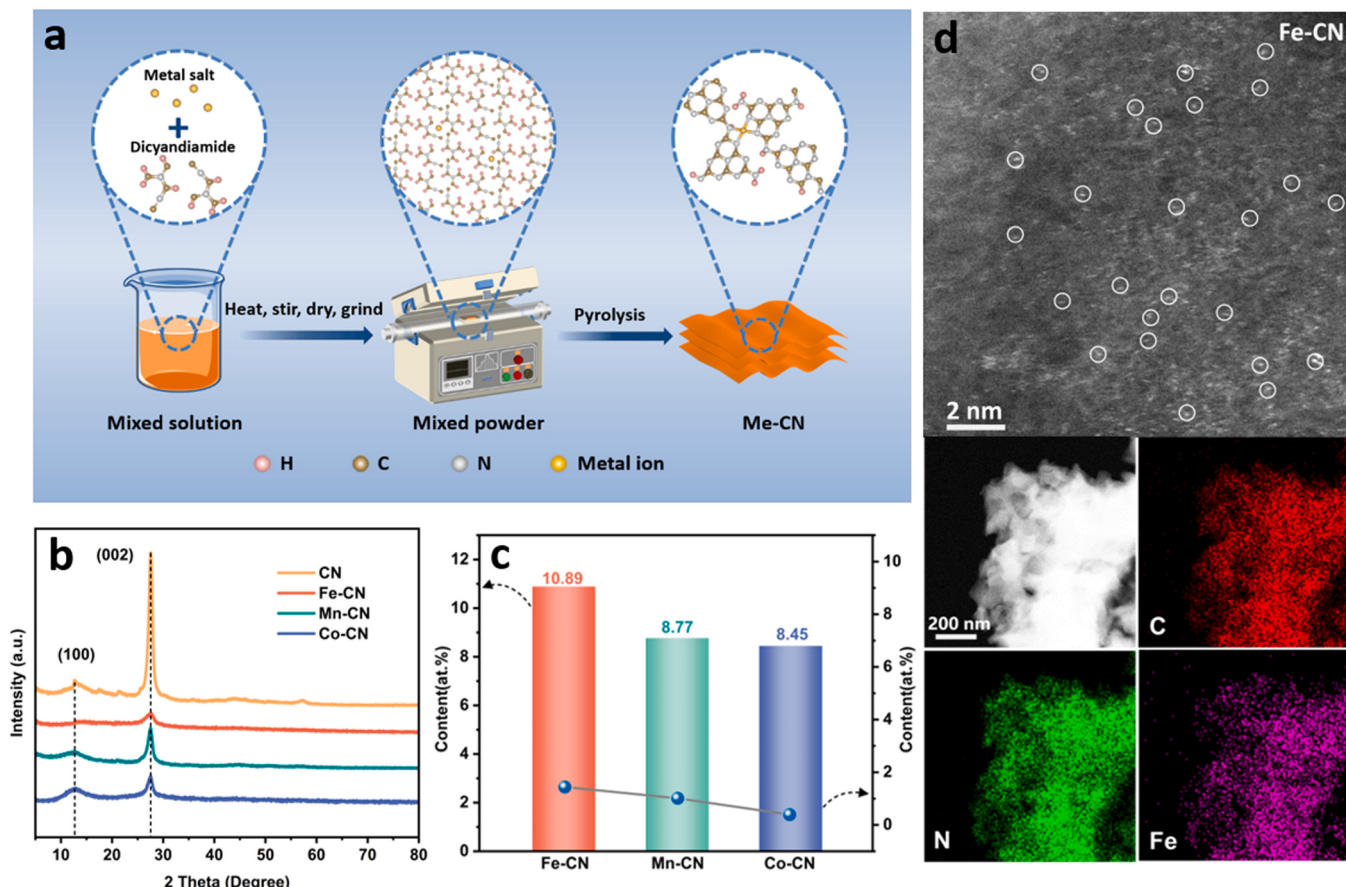


**Fig. 1.** (a) The preparation process of Me-CN. (b) XRD pattern. (c) Metal contents (at%) of Me-CN obtained by ICP-OES. (d) HAADF-STEM and elemental mapping images of Fe-CN.

### 3. Results and discussions

#### 3.1. Characterization of catalysts

The overall synthesis scheme of Me-CN was shown in Fig. 1a. Me-CN was prepared via mixing dicyandiamide with metal salts, followed by drying, and then thermally polymerizing under  $N_2$  atmosphere [26,27]. XRD of CN and Me-CN illustrated that the layered structure of CN was remained after doping metal species (Fig. 1b). All catalysts had two characteristic peaks at  $\sim 13.1^\circ$  (100 plane) and  $27.6^\circ$  (002 plane), corresponding to the interplanar stacking of the s-triazine unit and the stacking of aromatic fragment between the carbon nitride layers, respectively [28]. Compared to those of pure CN, the peak intensity of Me-CN was slightly decreased, indicating the decrease of crystallinity due to the perturbation of the stacked layers caused by metal atoms [29]. Additionally, no metal oxide clusters were observed in the XRD pattern, suggesting that metal atoms were highly dispersed and doped in CN, most likely in the form of metal-N bonds [30,31]. All samples presented similar FTIR spectra, verifying that the s-triazine structure of CN still preserved after doping atomic metal (Fig.S2). The peaks at 808 and  $1200\text{--}1650\text{ cm}^{-1}$  represented the bending vibration and stretching vibration of s-triazine ring, respectively, and the peaks at  $3000\text{--}3700\text{ cm}^{-1}$  were referred to the stretching vibration of  $-\text{NH}_2$  at the edge of s-triazine ring and  $-\text{OH}$  [32–34]. The peak intensities of Me-CN were significantly lower than those of CN, which was attributed to the disturbance of s-triazine ring induced by metal-N-C bonds [35]. No characteristic peaks of metal-N bonds were observed because of the extremely low metal contents. As shown in Fig. 1c, the metal contents of Me-CN were measured as 10.9, 8.8, and 8.5 at% for Fe-CN, Mn-CN, and Co-CN, respectively. All catalysts were stable during 30 min's PCO reaction. The maximum metal leach only accounted for 1.44, 1.01, and 0.39 at% of the total metal content in Fe-CN, Mn-CN, and Co-CN, respectively.  $N_2$  adsorption-desorption isotherms were conducted to obtain the information on  $S_{\text{BET}}$ , pore size and pore volume. All  $N_2$  adsorption-desorption isotherms were type III (Fig.S3).  $S_{\text{BET}}$  were

measured as 26.0, 24.4, 20.9 and  $13.7\text{ m}^2/\text{g}$  for CN, Fe, Co, Mn-CN, respectively. The doing of active metal slightly reduced the  $S_{\text{BET}}$ .

As depicted in high-angle annular dark-field scanning transmission electron microscopy (HAADF-STEM, Fig. 1d, Fig.S4), the atomic metals (bright dots with white circles) were observed clearly on CN, and no metal clusters were found [36]. Elemental mapping further confirmed the uniform distribution of C, N, and atomic metal on CN. More information about the detailed atomic structure of Me-CN was characterized by X-ray photoelectron spectroscopy (XPS). As shown in Fig.S5, there were common elements like C, N, and O in all Me-CN. The existence of O element was attributed to the surface-adsorbed  $\text{H}_2\text{O}$ . C1s spectrum of all catalysts could be deconvoluted into three peaks with binding energy of 284.8, 286.1, and 288.2 eV, corresponding to the amorphous C (C–C/C=C), C–O of surface absorbed- $\text{H}_2\text{O}$  and the  $\text{sp}^2$  hybridization in s-triazine units (N–C=N), respectively. N1s spectrum of all catalysts could be deconvoluted into four peaks with binding energy of 398.7 eV ( $\text{sp}^2$  hybrid N (C=N=C)), 399.1 eV (bridged N (N–(C)<sub>3</sub>)), 400.9 eV (N–H bond) and 404.3 eV ( $\pi\text{-}\pi^*$  excitation between stacked layers) [37,38]. The above results further confirmed that the structure of CN was not disrupted by the presence of atomic metals. In addition, Fe2p, Mn2p, and Co2p patterns (Fig.S6, Table S1) showed that Fe in Fe-CN existed in  $\equiv\text{Fe}(\text{II})$  and  $\equiv\text{Fe}(\text{III})$ , Mn in Mn-CN existed in  $\equiv\text{Mn}(\text{II})$ ,  $\equiv\text{Mn}(\text{III})$  and  $\equiv\text{Mn}(\text{IV})$ , and Co in Co-CN existed  $\equiv\text{Co}(\text{II})$  and  $\equiv\text{Co}(\text{III})$ , respectively [39–41].

To further obtain the precise coordination structure of Me-CN, X-ray absorption spectroscopy (XAS) was performed. The valence of metals could be verified by X-ray absorption near-edge structure (XANES, Fig. 2a-b, Fig.S7). Taking Fe-CN as an example, the near-edge absorption threshold of Fe-CN was located between  $\text{FeO}$  and  $\text{Fe}_2\text{O}_3$ , indicating that the average valence of Fe in Fe-CN was between +2 and +3. XANES results were consistent with the XPS characterization. In the Fe K-edge fourier transform extended X-ray absorption fine structure spectra (FT-EXAFS, Fig. 2c), the peak of Fe atoms in Fe-CN was located at  $\sim 1.6\text{ \AA}$ , which was different from the Fe–Fe peaks ( $\sim 2.2\text{ \AA}$ ) in the Fe foils and Fe–O peaks ( $\sim 1.4\text{ \AA}$ ) in the Fe oxides. The results also excluded the

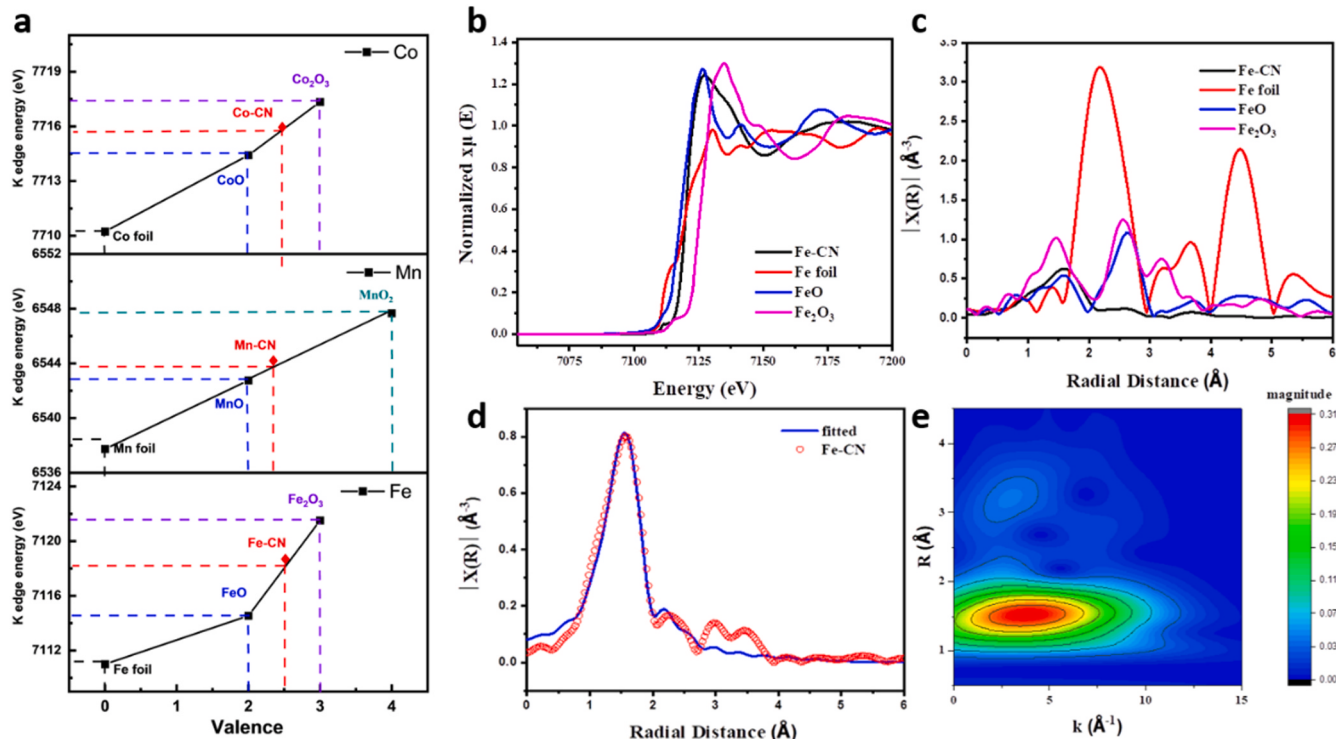


Fig. 2. (a) Relation between the metal K-edge absorption energy ( $E^0$ ) and valence states for Me-CN and reference materials. (b) XANES spectra at the relative Fe K-edge. (c) Fe K-edge FT-EXAFS spectra. (d) EXAFS in R-space and corresponding fitting curve. (e) Wavelet transforms for the  $k^3$ -weighted EXAFS signals of Fe-CN.

presence of  $\text{Fe}^0$  or Fe oxides clusters. The EXAFS in R-space (Fig. 2d) and wavelet transform (WT, Fig. 2e) further suggested that Fe–N bonds were formed in Fe-CN. The maximum intensity of Fe-CN appearing at  $\sim 4.0 \text{ \AA}^{-1}$  was assigned to the Fe–N bond, which was different with that of Fe foil ( $\sim 7.5 \text{ \AA}^{-1}$ ). As shown in Table S2, the coordination numbers of Fe, Mn, and Co with N atoms were all fitted as 4, and their bond lengths to N coordination were 2.10, 2.21, and 2.04  $\text{\AA}$ , respectively [42,43]. The above results verified that the atomic metals were successfully incorporated into the CN in the form of metal–N configurations.

### 3.2. Photocatalytic ozonation performances

OA was primarily selected as a model pollutant to evaluate the PCO performance of Me-CN. As shown in Fig. 3a, Me-CN exhibited the greater activity for OA removal than that of CN during PCO process. After 30 min's reaction, OA removals were 98.5%, 98.9%, and 93.7% in PCO/Fe-CN, PCO/Mn-CN, and PCO/Co-CN, respectively, which were much higher than that of PCO/CN (89.2%). In addition, their first-order kinetic rate constants were in the order of PCO/Fe-CN ( $0.228 \text{ min}^{-1}$ ) > PCO/Mn-CN ( $0.154 \text{ min}^{-1}$ ) > PCO/Co-CN ( $0.097 \text{ min}^{-1}$ ) > PCO/CN ( $0.078 \text{ min}^{-1}$ ). The normalized k by metal content was  $20.9 (\text{min}^* \text{g})^{-1}$  for PCO/Fe-CN,  $17.5 (\text{min}^* \text{g})^{-1}$  for PCO/Mn-CN and  $11.4 (\text{min}^* \text{g})^{-1}$  for PCO/Co-CN process. Additionally, the normalized k by  $S_{\text{BET}}$  were also in the order of PCO/Fe-CN ( $0.093 \text{ min}^{-1} \text{m}^{-2}$ ) > PCO/Mn-CN ( $0.074 \text{ min}^{-1} \text{m}^{-2}$ ) > PCO/Co-CN ( $0.070 \text{ min}^{-1} \text{m}^{-2}$ ) > PCO/CN ( $0.030 \text{ min}^{-1} \text{m}^{-2}$ ). The above results indicated that the variations in OA removal were induced by the inherent properties of metal–N–C. Average quantum efficiencies (AQEs) of different catalytic systems were evaluated. They were calculated as 2.96%, 13.48%, 8.26%, 4.56% for CN, Fe-CN, Mn-CN and Co-CN, respectively, suggesting that doping of metal species would enhance the efficiency of photocatalytic activity.

To further explore the role of metals in CN, comparative degradations were carried out using Fe-CN as an example (Fig. 3b). OA removals were less than 15.0% either by sole ozonation, solar light irradiation or Fe-CN adsorption. In addition, the combination of  $\text{O}_3$  and Fe-CN hardly

enhanced OA removal because of the extremely low Lewis acid sites (positively related to Fe content). Surprisingly, the incorporation of Fe species enhanced PC activity of CN, achieving 64.7% OA removal in PC/Fe-CN process, but only 6.0% OA removal was obtained in PC/CN process. OA degradation was significantly improved after coupling the ozonation with PC processes, and the PCO/Fe-CN (98.5%) process performed better than PCO/CN (89.2%).

The order of photocatalytic (PC) activity was: PC/Fe-CN > PC/Mn-CN > PC/Co-CN > PC/CN, which was consistent with the results of PCO processes (Fig. S8). The above results suggested that the  $e_{\text{cb}}$  utilization rate was crucial to the PCO process. The synergy factors ( $\eta$ ) were calculated to emphasize the advantage of PCO process (Fig. 3c, Table S3).  $\eta$  decreased in the order of PCO/Fe-CN (24.04) > PCO/Co-CN (15.79) > PCO/CN (13.45) > PCO/Mn-CN (3.24). It was interesting that Mn-CN had the high OA degradation efficiency but the lowest synergistic effect, suggesting that there existed different  $\text{O}_3$  activation pathways depending on metal species and Mn-CN had lowest ability in utilizing  $e_{\text{cb}}$ . The influence of initial pH on OA removal was also explored. As shown in Fig. 3d, OA removal decreased as the pH increased from 3.8 to 9 because of the promotion of  $\bullet\text{OH}$  formation induced by  $\text{H}^+$  in PCO reaction (Eqs. 1–2) [44]. Furthermore, the ability of PCO/Fe-CN process in degrading various pollutants (Fig. 3e) was tested, including chloramphenicol (CAP), ibuprofen (IBP), flufenic acid (FF), atrazine (ATZ), ketoprofen (KTP), sulfamethoxazole (SMX), sulfamethazine (SM2), carbamazepine (CBZ), and metronidazole (MTZ). The removals of KTP, CBZ, SMX, SM2, FF, CAP, MTZ, and IBP in the PCO/Fe-CN process reached 95–100% after 30 min's reaction. Even for the most refractory compound like ATZ, its removal reached 81.7%. The findings indicated that PCO/Fe-CN process demonstrated a broad applicability in the degradation of various organic compounds found in wastewater. In addition, we compared the catalytic performance of Me-CN with the reported catalysts in PCO process (Table S4), and all the catalysts in this study displayed the higher OA removal and k values in a shorter time. This suggested a bright prospect of Me-CN based PCO process (Fig. 3f).

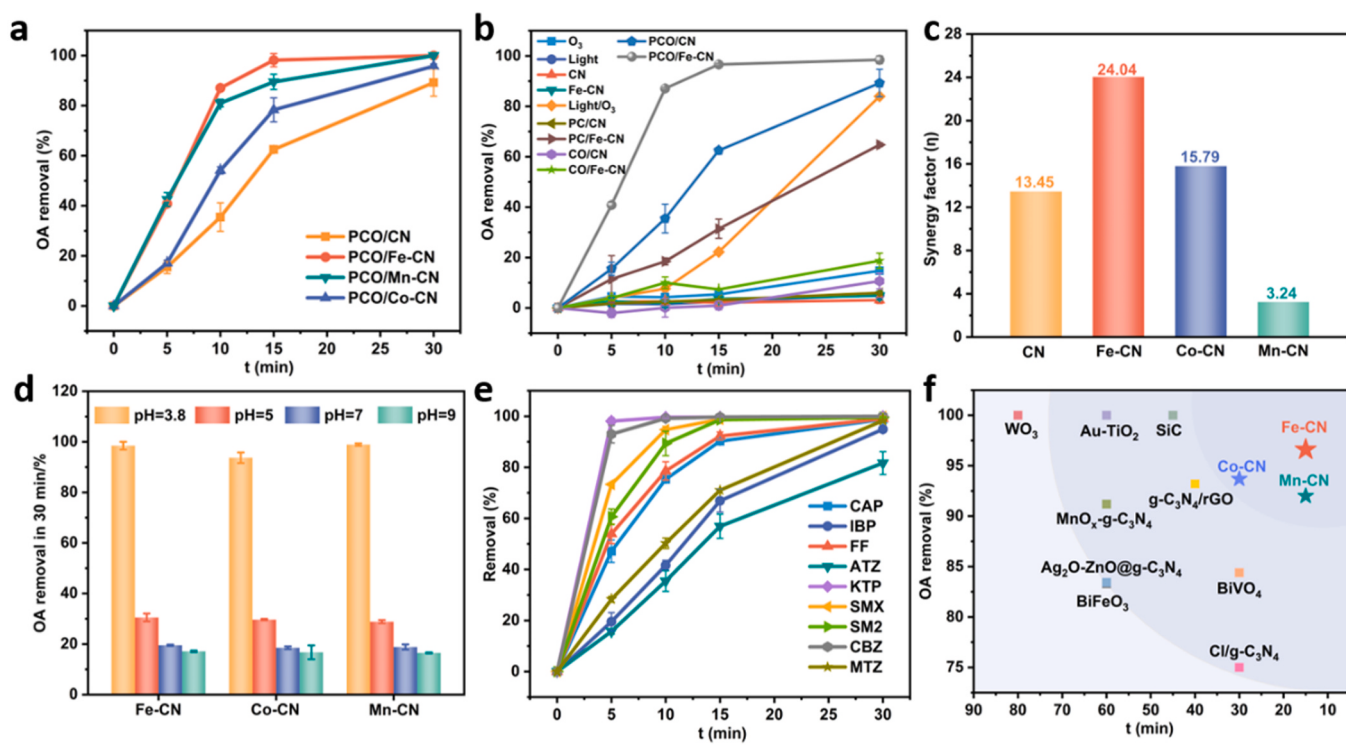


**Fig. 3.** (a) Influence of metal type on OA removal. (b) Systematically comparison of OA degradation by PCO/Fe-CN process. (c) Synergy factor ( $\eta$ ) of all samples. (d) Influence of pH on different PCO processes. (e) Degradation of typical pollutants by PCO/Fe-CN. (f) Comparison of pollutant degradation percentage and time.

### 3.3. Reaction mechanism

As a highly refractory pollutant, OA could not be degraded by  $O_3$  ( $k_{OA, O_3} = 0.039 \text{ M}^{-1} \text{ s}^{-1}$ ) and  $h_{cb}^+$  but it was highly reactive with  $\bullet\text{OH}$  ( $k_{OA, \bullet\text{OH}} = 5.5 \pm 0.5 \times 10^7 \text{ M}^{-1} \text{ s}^{-1}$ ), which was an important product from  $O_3$  activation either by  $e_{cb}^-$  or inherent electron of metal species [45, 46]. To elucidate the OA degradation mechanism,  $\text{HCO}_3^-$ ,  $\text{BrO}_3^-$ , and  $\text{PO}_4^{3-}$  were selected to investigate the contribution of  $\bullet\text{OH}$ , electrons, and Lewis acid sites (LAS), respectively [47–49]. As shown in Fig. 4a, after adding  $\text{HCO}_3^-$ , great inhibition on OA removals was found in PCO/Fe-CN, PCO/Mn-CN, and PCO/Co-CN processes, indicating the key role of  $\bullet\text{OH}$  in degrading OA.  $\text{KBrO}_3$  was an electron scavenger. Normally, the reductive  $e_{cb}^-$  could either migrate to the surface to activate  $O_3$  directly or be stored by metal species for the subsequent  $O_3$  activation. Experimental results suggested that  $\text{BrO}_3^-$  had a minimal impact on PCO/Fe-CN and PCO/Co-CN processes, but exhibited greater inhibition on PCO/Mn-CN process (from 98.9% to 90.9%), reflecting that  $e_{cb}^-$  was less likely to react with Mn species. The presence of  $\text{PO}_4^{3-}$  reduced OA removal in all PCO/Me-CN process and the greatest inhibition was also observed for PCO/Mn-CN process. Typically,  $\text{PO}_4^{3-}$  was recognized as Lewis base and it could shelter LAS to inhibit the subsequent  $O_3$  activation. As shown in Fig.S9 and Table S5, Mn-CN (30.3  $\mu\text{mol/g}$ ) had a greater LAS than that of Fe-CN (16.8  $\mu\text{mol/g}$ ) and Co-CN (14.8  $\mu\text{mol/g}$ ) [50]. It could be inferred that LAS played a more important role in activating  $O_3$  in PCO/Mn-CN process compared to other PCO/Me-CN processes.

$R_{CT}$  value was employed to assess the  $\bullet\text{OH}$  exposure rate (Fig. 4b) [51, 52]. According to the calculated parameters exhibited in Fig.S10

and Table S6, the order of  $R_{CT}$  was  $\text{PCO/Fe-CN} (7.5 \times 10^{-6}) > \text{PCO/Mn-CN} (6.6 \times 10^{-6}) > \text{PCO/Co-CN} (5.2 \times 10^{-6}) > \text{PCO/CN} (3.1 \times 10^{-6})$ , which was positively correlated with their OA removals. The higher  $R_{CT}$  value suggested a greater  $\bullet\text{OH}$  generating rate. The above results underlined the excellent ability of PCO/Me-CN in producing  $\bullet\text{OH}$ .

Generally, there were two  $O_3$  activation pathways for metal-based catalysts during PCO process, including a traditional catalytic ozonation route where the metal center directly delivered its intrinsic electrons to  $O_3$  (Eqs.11–12) and a pathway where  $O_3$  was activated by  $e_{cb}^-$  (Eqs.13–14). For the sake of exploring  $O_3$  activation pathways, electron paramagnetic resonance (EPR) was employed. As depicted in Fig. 4c,  $\bullet\text{OH-DMPO}$  adduct showed the quartet peaks with intensity ratio of 1:2:2:1 and their hyperfine splitting couplings were  $a_N = a_H = 14.9 \text{ G}$  [53]. It should be noted that the yield of  $\bullet\text{OH}$  reflected by EPR was in the order of  $\text{Co-CN} < \text{Fe-CN} < \text{Mn-CN}$ , which was inconsistent with the OA removals and the  $R_{CT}$  value.  $O_3$  exposure level was vital for  $\bullet\text{OH}$  generation. During PCO process,  $O_3$  was continuously bubbling into solution, therefore, it was excessive in the PCO system. But as for the EPR testing, the dissolved  $O_3$  was rapidly consumed by catalyst. When  $e_{cb}^-$  was excited, the remaining  $O_3$  failed to make full use of  $e_{cb}^-$ , which resulted in the abnormal order of  $\bullet\text{OH}$  production. Fig. 4d indicated that the characteristic peaks of  $\bullet\text{O}_2\text{-DMPO}$  complexes showed sextet signals (hyperfine splitting couplings were  $a_N = 14.2 \text{ G}$ ,  $a_H^\beta = 11.4 \text{ G}$ , and  $a_H^\gamma = 1.2 \text{ G}$ ) [54]. The yield of  $\bullet\text{O}_2$  increased in the order of  $\text{Fe-CN} < \text{Co-CN} < \text{Mn-CN}$ .  $\bullet\text{O}_2$  was generated from the one electron reduction of  $O_2$  ( $O_2 + e^- \rightarrow \bullet\text{O}_2$ ). The less  $\bullet\text{O}_2$  in PCO/Fe-CN and PCO/Co-CN processes demonstrated that fewer  $e_{cb}^-$  were able to reduce  $O_2$  into  $\bullet\text{O}_2$  due to the

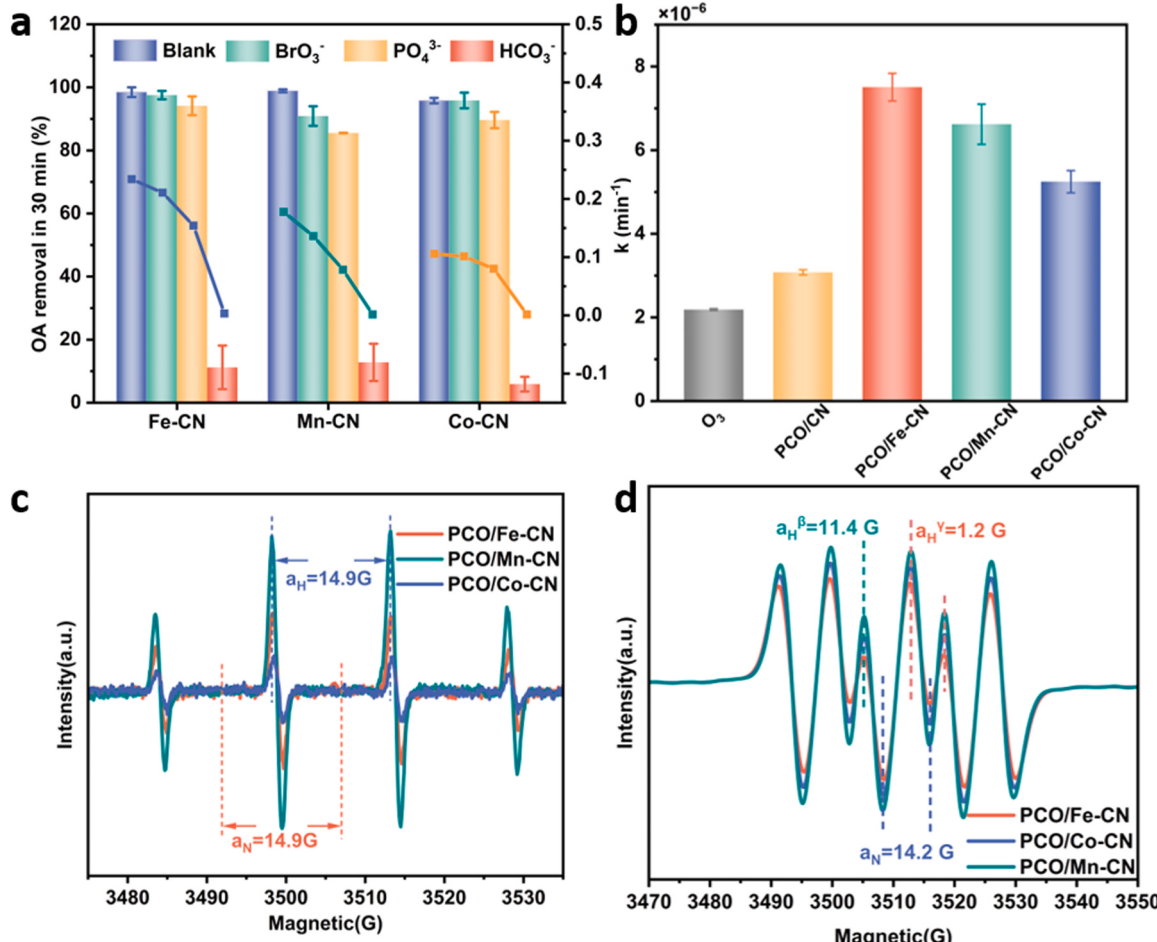


Fig. 4. (a) Influence of scavenger on different PCO processes. (b)  $R_{CT}$  value of different catalytic systems processes. (c) EPR pattern of  $\bullet\text{OH-DMPO}$  adducts. (d) EPR pattern of  $\bullet\text{O}_2\text{-DMPO}$  adducts.

rapid consumption of  $e_{cb}^-$  by Fe-N-C and Co-N-C units. While the greatest amount of  $\bullet\text{O}_2$  in PCO/Mn-CN indicated the low efficiency of Mn-N-C in storing  $e_{cb}^-$ .

Based on the above results, the main  $\text{O}_3$  activation pathway in three PCO processes was deduced. For PCO/Mn-CN process,  $\text{O}_3$  was activated by the continuous sacrifice of electron from  $\text{Mn}^{2+}/\text{Mn}^{3+}/\text{Mn}^{4+}$  redox cycle. Meanwhile, the direct reaction between  $\text{O}_3$  and  $e_{cb}^-$  could also activate  $\text{O}_3$ . As for Fe-CN and Co-CN based PCO processes, the metal sites would serve as " $e_{cb}^-$  depot".  $e_{cb}^-$  was captured by Co-N-C and Fe-N-C unit and refresh the  $\text{Fe}^{3+}$  and  $\text{Co}^{3+}$  to  $\text{Fe}^{2+}$  and  $\text{Co}^{2+}$ , respectively (Eq.15). Then,  $\text{O}_3$  was activated by the reductive Fe and Co. This process was driven by the  $e_{cb}^-$ .



Cycling tests and the change of band gap ( $E_g$ ) were investigated to demonstrate the different function of Me-N-C. As exhibited in Fig. 5a, Fe-CN and Co-CN still had a remarkable activity after four successive runs but OA removal in PCO/Mn-CN significantly declined after the second run. Meanwhile, the change of band structure was also explored.  $E_g$  of Fe-CN, Co-CN, and Mn-CN was 2.61, 2.57, and 2.72 eV, respectively, which were all smaller than that of CN (2.79 eV), indicating the existence of Me-N-C units enhanced light absorption and the  $h_{vb}^+ - e_{cb}^-$  yields of CN (Fig.S11-13) [21]. Photoluminescence (PL) and fluorescence lifetime spectroscopy (TRPL) tests were used to study the  $h_{vb}^+ - e_{cb}^-$  separation efficiency. As depicted in Fig.S14, the peak order of PL spectrum was: Fe-CN < Co-CN < Mn-CN < CN. The above results indicated that the doping

of metals accelerated the migration of photogenerated carriers in CN and suppressed the recombination of  $h_{vb}^+ - e_{cb}^-$ . Furthermore, the average lifetimes of photo-generated carriers measured by TRPL were 3.79, 4.41, 4.30, and 6.12 ns for Fe-CN, Co-CN, Mn-CN and CN, respectively. The shorter carrier lifetime of metal doped CN than that of CN suggested that  $e_{cb}^-$  could be consumed by metal sites. And Mn-CN had the greater carrier lifetime over those of Fe-CN and Co-CN, indicating that Mn had the lower activity with  $e_{cb}^-$ , which was consistent with the former proposal. It was found that the conduction band (CB) position of Mn-CN shifted downward from  $-0.99$  to  $-0.74$  eV after two PCO reactions while that of Fe-CN and Co-CN had insignificant change. Considering the negligible metal leaching, the activity decrease of Mn-CN was attributed to the alteration of their band structure during PCO process. Generally, band structure of metal doped CN was highly related to the valence of metal species. Because of the efficient utilization of  $e_{cb}^-$  by Fe-N-C and Co-N-C, the valence of Fe and Co had no remarkable change, therefore, both catalytic activity and band structure of Fe-CN and Co-CN were stable. The poor stability of Mn-CN further indicated the inefficient utilization of  $e_{cb}^-$  by Mn-N-C (Fig. 5b, Fig.S15). During PCO/Mn-CN process, parts of  $\text{O}_3$  were activated with Mn providing its internal electrons. The in-situ electrochemical tests on rotating ring-desk electrodes (RRDE) were carried to explore the electron transfer numbers (n). As depicted in Fig. S16, the calculated n values were 3.9, 3.5, 3.1 and 2.9 for Fe-CN, Mn-CN, Co-CN and CN, respectively, which was positively related with the PCO activity trend. The above results verified that the doping of atomic metal species could enhance the interfacial electron transfer process and  $\text{O}_3$  activation. To further investigate the behavior of  $e_{cb}^-$  in each Me-CN, more electrochemical characterizations were performed. After being irradiated,  $e_{cb}^-$  were separated from  $h_{vb}^+$  and then transferred to the electrode surface, exhibiting the photocurrent signal [55,56]. As shown in Fig. 5c, comparing with that of CN, Fe-CN and Co-CN had the smaller photocurrent but Mn-CN exhibited the greater photocurrent, which further suggested that  $e_{cb}^-$  could be well restored by Fe-N-C and Co-N-C

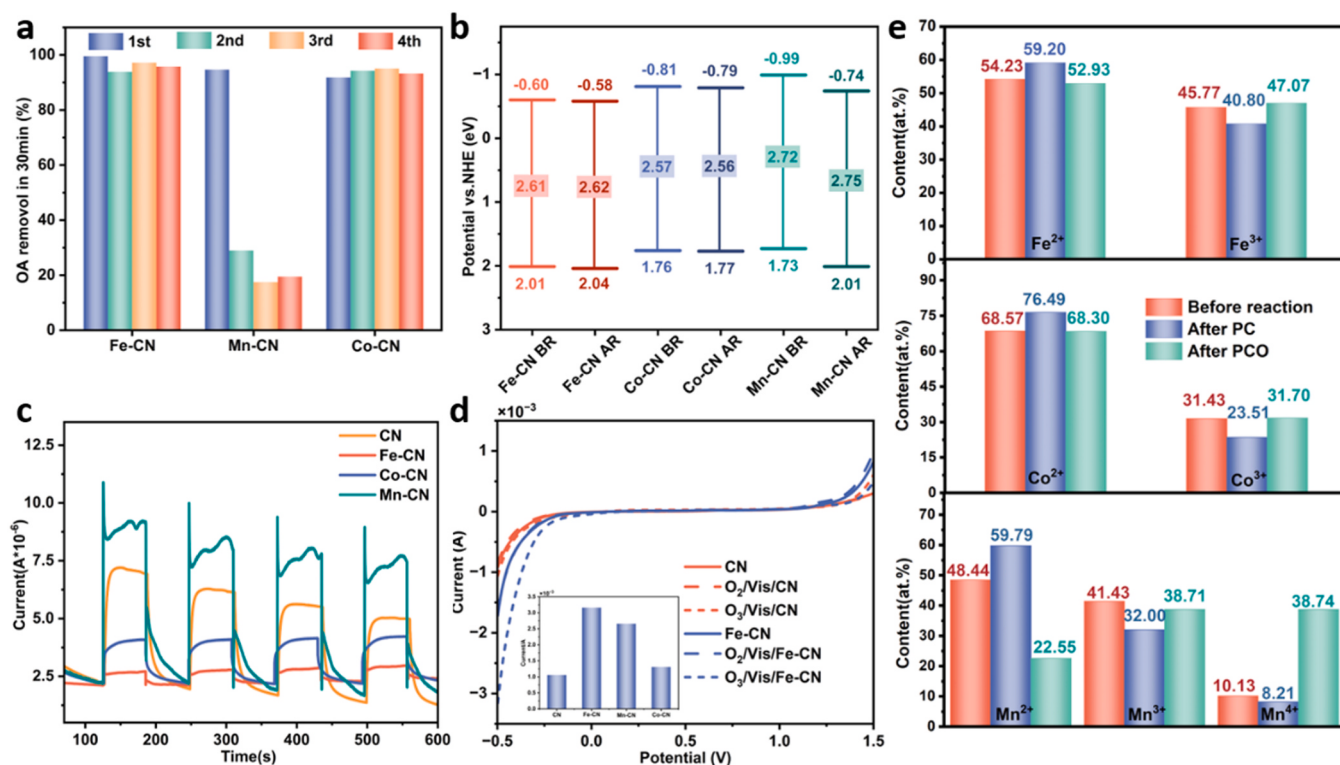


**Fig. 5.** (a) Cycling stability of Me-CN for OA degradation. (b) Band structure of Me-CN before reaction (BR) and after twice PCO reactions (AR). (c) Photocurrent curves. (d) Linear sweep voltammetry curve (LSV) characterization and initial current of different PCO processes. (e) Percentage of metal ions in Me-CN before and after PC/PCO reaction.

units but it was difficult to be captured by Mn-CN. In addition, the photocurrent values of all catalysts became smaller after introducing  $O_3$  (Fig.S17), corresponding to the consumption of  $e_{cb}^-$  by  $O_3$ . Meanwhile, linear sweep voltammetry (LSV, Fig. 5d) were performed to reveal the interfacial charge transfer ability of the photocatalysts. The initial current values of all Me-CN were larger than that of CN, which indicated that they had stronger interfacial charge transfer, especially for Fe-CN. The initial current values of  $O_2$ /Vis/Me-CN had only a slight increase compared to the sole catalysts. However, after introducing  $O_3$ , the initial current values of  $O_3$ /Vis/Fe-CN,  $O_3$ /Vis/Co-CN and  $O_3$ /Vis/Mn-CN were significantly increased to  $1.5 \times 10^{-3}$ ,  $5.7 \times 10^{-4}$  and  $1.6 \times 10^{-3}$  A, respectively (Fig.S18). The above results showed that the existence of  $O_3$  significantly enhanced the interfacial electron migration [57].

The restoration of  $e_{cb}^-$  was unveiled by XPS. As shown in Fig. 5e, light irradiation could reduce  $\equiv$ Fe(III) to  $\equiv$ Fe(II),  $\equiv$ Co(III) to  $\equiv$ Co(II), and  $\equiv$ Mn(III) to  $\equiv$ Mn(II) in Fe-CN, Co-CN, and Mn-CN, respectively. The percentage of divalent metal increased in all Me-CN after PC reaction, with  $\equiv$ Fe(II)% increased from 54.23% to 59.20%,  $\equiv$ Co(II)% increased from 68.57% to 76.49%, and  $\equiv$ Mn(II)% increased from 48.44% to 59.79%, respectively. However, when referring to PCO reaction, there was a small increase of  $\equiv$ Fe(III)% and  $\equiv$ Co(III)% (less than 8.50%) while a more remarkable accumulation of oxidized metal species was found for Mn-CN (37.24%). The above results were predictable from the redox potential of active metal ( $E^0(Co^{3+}/Co^{2+}) = 1.81$  V,  $E^0(Fe^{3+}/Fe^{2+}) = 0.77$  V,  $E^0(Mn^{3+}/Mn^{2+}) = 1.51$  V,  $E^0(Mn^{4+}/Mn^{3+}) = 0.15$  V). The  $Mn^{4+}/Mn^{3+}$  redox couple exhibited an extremely low redox potential, suggesting the difficult conversion of  $Mn^{4+}$  to  $Mn^{3+}$  by  $e_{cb}^-$ .

Based on the above discussion, the main pathway of  $O_3$  activation in various PCO/Me-CN systems could be summarized as following: For PCO/Fe-CN and PCO/Co-CN,  $e_{cb}^-$  was first used to reduce Fe and Co which was indexed as the store of  $e_{cb}^-$ . Then the reduced Fe and Co in Me-CN conveyed the stored  $e_{cb}^-$  to activate  $O_3$  into  $\bullet OH$ . In PCO/Mn-CN process, there existed two  $O_3$  activation paths. The main route was driven by the sacrifice of electrons low-valence Mn. The secondary path was the reduction of  $O_3$  by  $e_{cb}^-$ . Due to its poor utilization efficiency of  $e_{cb}^-$ , the high-valence Mn constantly accumulated.

### 3.4. Theoretical Calculations

To further investigate the reaction between  $O_3$  and Me-N-C units, Me-CN with the s-triazine ring as the basic unit was constructed for DFT calculations. Atomic metals were anchored by four N atoms in the interstices of adjacent s-triazine rings according to the results of XAFS. As shown in Table S7, the average bond lengths of Fe-N, Co-N, and Mn-N for the optimized configurations were calculated as 1.99, 2.07, and 2.13 Å, respectively, and less than 5.6% deviation was found with the results of EXAFS. The adsorption energies of  $O_3$  ( $E_{ad-O_3}$ ) on various Me-CN were investigated, with Mn-CN (-3.31 eV) exhibited the highest, followed by Fe-CN (-3.12 eV) and then Co-CN (-2.09 eV), which was consistent with the trend of  $O_3$  concentration and HCO process (Fig. S19). Besides, the differential charge density of all adsorption configurations clearly demonstrated that electrons were transferred from Me-N-C sites to the adsorbed  $O_3$ , corresponding to the reductive activation of  $O_3$  (Fig. 6a) [58,59].

Basing on the aforementioned deduction, two different  $O_3$  activation pathways were designed, which were dominated by photo-activation effects (path 1) and metal active site effects (path 2), respectively (Fig. 6b-d) [60,61]. In path 1,  $O_3$  was activated through the photo-induced processes.  $O_3$  was first absorbed by Me-CN (Eq.15). Then, Me-CN absorbed photons and the generated  $e_{cb}^-$  transferred to the surface bonded  $O_3$ . The excited  $*O_3$  was easily combined with  $H^+$  to form  $*O_3H$ , which eventually dissociated into  $\bullet OH$  (Eqs.16-17). There existed two transition states for conveying  $O_3$  into  $\bullet OH$  for Eq.16 and Eq.17, which were named as TS1 and TS2, respectively. In path 2, the metal species donated its electron to surface bonded  $O_3$ , generating surface atomic oxygen ( $*O$ , Eq.18).  $*O$  was highly reactive with an oxidation potential of 2.43 eV and it would oxidize surface  $H_2O$  into  $\bullet OH$  (Eqs.19-20) [62]. Similarly, there existed two transition states for  $\bullet OH$  generation for Eq.19 and Eq.20, which were named as TS3 and TS4, respectively.

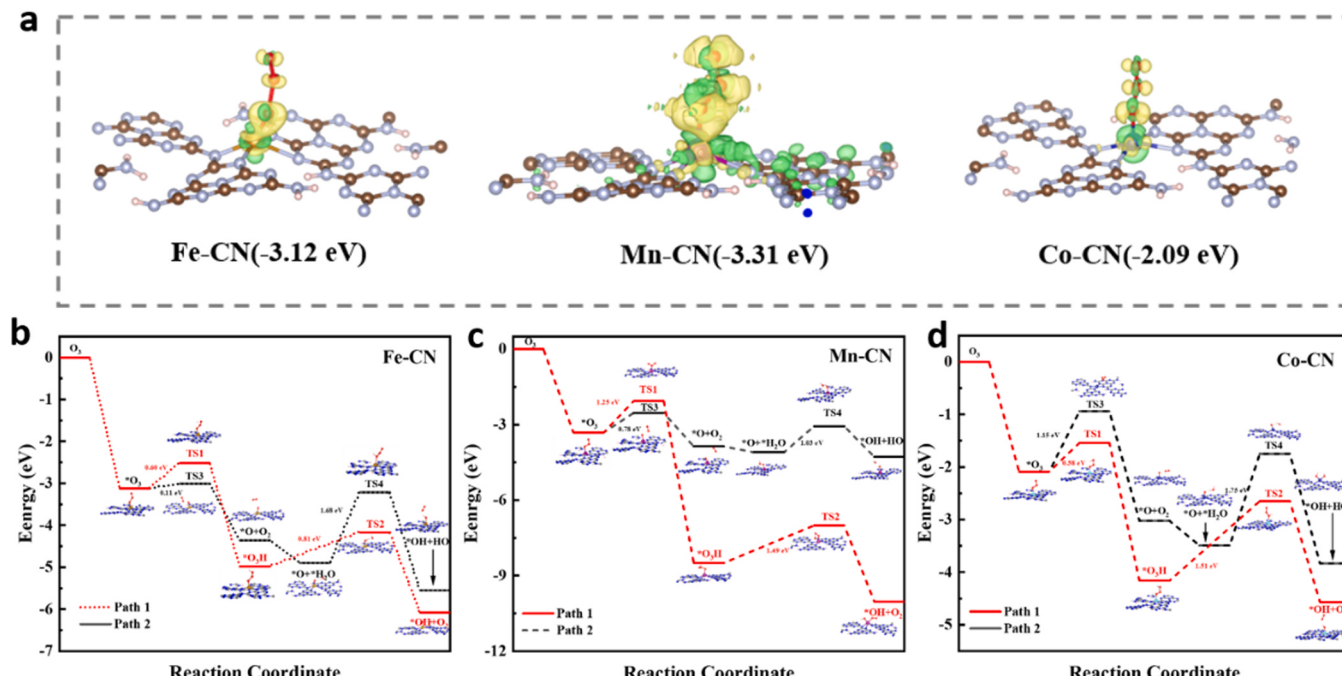


Fig. 6. (a) Differential charge densities of  $O_3$  adsorption model on Me-CN, the inserted values were the  $E_{ad-O_3}$  (Yellow indicated electrons accumulation, green indicated electrons depletion). Energy comparison of Me-CN with different metal-N catalytic sites on (b) Fe-CN, (c) Mn-CN, and (d) Co-CN.



To identify the most probable pathway for  $O_3$  activation as well as determine the rate-limiting step, the comparison of the energy barriers ( $\Delta E$ ) associated with each transition state was made. In path 1, the rate-determining step for  $O_3$  activation was the dissociation of  $*O_3H$  of TS2, and  $\Delta E$  decreased in the order of  $\Delta E_{\text{path1/Fe-CN}} (0.81 \text{ eV}) < \Delta E_{\text{path1/Mn-CN}} (1.49 \text{ eV}) < \Delta E_{\text{path1/Co-CN}} (1.51 \text{ eV})$ . Similarly, the rate-limiting step in path 2 was oxidation of  $H_2O$  by  $*O$  in TS4, and  $\Delta E$  was in the order of  $\Delta E_{\text{path2/Mn-CN}} (1.03 \text{ eV}) < \Delta E_{\text{path2/Fe-CN}} (1.68 \text{ eV}) < \Delta E_{\text{path2/Co-CN}} (1.75 \text{ eV})$ . Obviously, the activations of  $O_3$  by Fe-CN and Co-CN during PCO process were likely to proceed in path 1 and the activations of  $O_3$  by Mn-CN mainly proceeded in path 2, which was consistent with former deduce. By comparing the rate limit steps, we found that  $\Delta E$  was in the order of  $\Delta E_{\text{path1/Fe-CN}} (0.81 \text{ eV}) < \Delta E_{\text{path2/Mn-CN}} (1.03 \text{ eV}) < \Delta E_{\text{path1/Co-CN}} (1.51 \text{ eV})$ , which was positively related with their activity trend. Therefore, the different in catalytic activity of Me-CN in PCO process was originated from the great difference of metal-N-C unit in activating  $O_3$ . The Fe-N-C and Co-N-C units were proven to be highly effective in enhancing water purification efficiency by serving as electron transport channels.

#### 4. Conclusions

Aromatic Fe, Co, and Mn were anchored in g-C<sub>3</sub>N<sub>4</sub> in the form of Me-N-C configuration and used to boost PCO process for OA removal. The activity trend of Me-CN was in the order of: Fe-CN (98.5%, 0.228 min<sup>-1</sup>) > Mn-CN (98.9%, 0.154 min<sup>-1</sup>) > Co-CN (93.7%, 0.097 min<sup>-1</sup>).  $\bullet OH$  was the main reactive species accounting for OA degradation. Although all Me-CN exhibited high activity than pure CN, their unique characteristics led to different behaviors in the process. Fe-N-C and Co-N-C could act as electron transfer channels to restore  $e_{cb}$  for the subsequent  $O_3$  activation, but Mn-N-C failed to realize such reaction. Two different  $O_3$  activation pathways were verified by experimental results and DFT calculation. In PCO/Fe-CN and PCO/Co-CN processes, light irradiation and  $O_3$  demonstrated a significant synergistic effect, whereas in the Mn-CN process, they exerted independent effects with  $\bullet OH$  formation occurring predominantly through the electron donation from Mn sites. This study offered valuable insights for exploring the mechanism of single-atom catalysts in PCO process.

#### CRediT authorship contribution statement

**Xukai Li:** Supervision. **Weirui Chen:** Writing – original draft, Supervision, Methodology, Investigation. **Gaozu Liao:** Supervision. **Yushan Tan:** Methodology, Investigation, Conceptualization. **Laisheng Li:** Writing – review & editing, Supervision, Funding acquisition. **Jianbing Wang:** Resources, Software, Writing – review & editing. **Jing Wang:** Supervision, Funding acquisition. **Yiming Tang:** Supervision.

#### Declaration of Competing Interest

The authors declare that they have no known competing financial interests or personal relationships that could have appeared to influence the work reported in this paper.

#### Data Availability

No data was used for the research described in the article.

#### Acknowledgments

This study was funded by National Natural Science Foundation (52200016, 52000079, 51978288, 22076050 and 51978658), Guangdong Basic and Applied Basic Research Foundation (2021A1515111143, 2024A1515011864) and Guangzhou Basic and Applied Basic Research Foundation (2024A04J9934).

#### Appendix A. Supporting information

Supplementary data associated with this article can be found in the online version at doi:10.1016/j.apcatb.2024.124005.

#### References

- [1] Y.-d Chen, X. Duan, X. Zhou, R. Wang, S. Wang, N.-q Ren, S.-H. Ho, Advanced oxidation processes for water disinfection: features, mechanisms and prospects, *Chem. Eng. J.* (2021) 409.
- [2] A. Saravanan, V.C. Deivayanai, P.S. Kumar, G. Rangasamy, R.V. Hemavathy, T. Harshana, N. Gayathri, K. Alagumalai, A detailed review on advanced oxidation process in treatment of wastewater: mechanism, challenges and future outlook, *Chemosphere* 308 (2022) 136524. Pt 3.
- [3] S. Gao, Z. Zhao, Y. Xu, J. Tian, H. Qi, W. Lin, F. Cui, Oxidation of sulfamethoxazole (SMX) by chlorine, ozone and permanganate—a comparative study, *J. Hazard Mater.* 274 (2014) 258–269.
- [4] X. Li, L. Fu, F. Chen, S. Zhao, J. Zhu, C. Yin, Application of heterogeneous catalytic ozonation in wastewater treatment: an overview, *Catalysts* 13 (2) (2023).
- [5] B. Wang, H. Zhang, F. Wang, X. Xiong, K. Tian, Y. Sun, T. Yu, Application of heterogeneous catalytic ozonation for refractory organics in wastewater, *Catalysts* 9 (3) (2019).
- [6] J. Nawrocki, B. Kasprzyk-Hordern, The efficiency and mechanisms of catalytic ozonation, *Appl. Catal. B Environ.* 99 (1–2) (2010) 27–42.
- [7] E. Issaka, J.N. Amu-Darko, S. Yakubu, F.O. Paphounda, N. Ali, M. Bilal, Advanced catalytic ozonation for degradation of pharmaceutical pollutants—a review, *Chemosphere* 289 (2022) 133208.
- [8] J. Wang, H. Chen, Catalytic ozonation for water and wastewater treatment: recent advances and perspective, *Sci. Total Environ.* 704 (2020) 135249.
- [9] W. Chen, H. He, J. Liang, X. Wei, X. Li, J. Wang, L. Li, A comprehensive review on metal based active sites and their interaction with O(3) during heterogeneous catalytic ozonation process: types, regulation and authentication. *J. Hazard Mater.* 443 (2023) 130302 (Pt B).
- [10] D. Wang, Y. He, Y. Chen, F. Yang, Z. He, T. Zeng, X. Lu, L. Wang, S. Song, J. Ma, Electron transfer enhancing the Mn(II)/Mn(III) cycle in MnO/CN towards catalytic ozonation of atrazine via a synergistic effect between MnO and CN, *Water Res.* 230 (2023) 119574.
- [11] B. Yang, B. Guan, Synergistic catalysis of ozonation and photooxidation by sandwich structured MnO(2)-NH(2)/GO/p-C(3)N(4) on cephalexin degradation, *J. Hazard Mater.* 439 (2022) 129540.
- [12] T.-Q. Yang, T.-Y. Ning, B. Peng, B.-Q. Shan, Y.-X. Zong, P. Hao, E.-H. Yuan, Q.-M. Chen, K. Zhang, Interfacial electron transfer promotes photo-catalytic reduction of 4-nitrophenol by Au/Ag2O nanoparticles confined in dendritic mesoporous silica nanospheres, *Catal. Sci. Technol.* 9 (20) (2019) 5786–5792.
- [13] Y. Liu, D. Wu, S. Peng, Y. Feng, Z. Liu, Enhanced mineralization of dimethyl phthalate by heterogeneous ozonation over nanostructured Cu-Fe-O surfaces: Synergistic effect and radical chain reactions, *Sep. Purif. Technol.* 209 (2019) 588–597.
- [14] Y. Ding, Y. Shi, W. Xiong, J.H. Sun, C. Li, Y.Q. Zhang, J. Guo, Insights into N-Coordinated Bimetallic Site Synergy during NO Selective Catalytic Reduction by CO, *ACS Appl. Mater. Interfaces* 13 (48) (2021) 57182–57192.
- [15] Y. Nie, S. Xing, C. Hu, J. Qu, Efficient removal of toxic pollutants over Fe-Co/ZrO<sub>2</sub> bimetallic catalyst with ozone, *Catal. Lett.* 142 (8) (2012) 1026–1032.
- [16] M. Mehrjouei, S. Müller, D. Möller, A review on photocatalytic ozonation used for the treatment of water and wastewater, *Chem. Eng. J.* 263 (2015) 209–219.
- [17] J. Xiao, Y. Xie, H. Cao, Y. Wang, Z. Guo, Y. Chen, Towards effective design of active nanocarbon materials for integrating visible-light photocatalysis with ozonation, *Carbon* 107 (2016) 658–666.
- [18] Y. Tan, W. Chen, G. Liao, X. Li, J. Wang, Y. Tang, L. Li, Strategy for improving photocatalytic ozonation activity of g-C<sub>3</sub>N<sub>4</sub> by halogen doping for water purification, *Appl. Catal. B Environ.* 306 (2022).
- [19] H. Cao, J. Wang, J.-H. Kim, Z. Guo, J. Xiao, J. Yang, J. Chang, Y. Shi, Y. Xie, Different roles of Fe atoms and nanoparticles on g-C<sub>3</sub>N<sub>4</sub> in regulating the reductive activation of ozone under visible light, *Appl. Catal. B: Environ.* 296 (2021) 120362.
- [20] Z. Guo, Y. Xie, J. Xiao, Z. Zhao, Y. Wang, Z. Xu, Y. Zhang, L. Yin, H. Cao, J. Gong, Single-Atom Mn–N<sub>4</sub> Site-catalyzed peroxone reaction for the efficient production of hydroxyl radicals in an acidic solution, *J. Am. Chem. Soc.* 141 (2019) 12005–12010.
- [21] T. Chen, D. Yin, F. Zhao, K.K. Kyu, B. Liu, D. Chen, K. Huang, L. Deng, L. Li, Fabrication of 2D heterojunction photocatalyst Co-g-C<sub>3</sub>N<sub>4</sub>/MoS<sub>2</sub> with enhanced solar-light-driven photocatalytic activity, *N. J. Chem.* 43 (1) (2019) 463–473.
- [22] Q. Liu, J. Zhang, Graphene supported Co-g-C<sub>3</sub>N<sub>4</sub> as a novel metal-macrocyclic electrocatalyst for the oxygen reduction reaction in fuel cells, *Langmuir: ACS J. Surf. Colloids* 29 (11) (2013) 3821–3828.

[23] J.P. Perdew, K. Burke, M. Ernzerhof, Generalized gradient approximation made simpl, *Phys. Rev. Lett.* **77** (1996) 3865–3868.

[24] K. Momma, F. Izumi, VESTA3 for three-dimensional visualization of crystal, volumetric and morphology data, *J. Appl. Crystallogr.* **44** (6) (2011) 1272–1276.

[25] WANG, V.; XU, N.; LIU, J.-C.; TANG, G.; GENG, W.-T., VASPKIT: A User-Friendly Interface Facilitating High-Throughput Computing and Analysis Using VASP Code. arXiv 2019, 1908.08269.

[26] C. Chu, Q. Zhu, Z. Pan, S. Gupta, D. Huang, Y. Du, S. Weon, Y. Wu, C. Muhich, E. Stavitski, K. Domen, J.H. Kim, Spatially separating redox centers on 2D carbon nitride with cobalt single atom for photocatalytic H(2)O(2) production, *Proc. Natl. Acad. Sci. USA* **117** (12) (2020) 6376–6382.

[27] F. Chen, X.L. Wu, C. Shi, H. Lin, J. Chen, Y. Shi, S. Wang, X. Duan, Molecular Engineering toward Pyrrolic N-Rich M-N<sub>4</sub> (M = Cr, Mn, Fe, Co, Cu) Single-Atom Sites for enhanced heterogeneous Fenton-like reaction, *Adv. Funct. Mater.* **31** (13) (2021).

[28] J.-N. Zhu, X.-Q. Zhu, F.-F. Cheng, P. Li, F. Wang, Y.-W. Xiao, W.-W. Xiong, Preparing copper doped carbon nitride from melamine templated crystalline copper chloride for Fenton-like catalysis, *Appl. Catal. B: Environ.* **256** (2019).

[29] J. Wang, Y. Xie, G. Yu, L. Yin, J. Xiao, Y. Wang, W. Lv, Z. Sun, J.H. Kim, H. Cao, manipulating selectivity of hydroxyl radical generation by single-atom catalysts in catalytic ozonation: surface or solution, *Environ. Sci. Technol.* **56** (24) (2022) 17753–17762.

[30] Y. Bai, Y. Zheng, Z. Wang, Q. Hong, S. Liu, Y. Shen, Y. Zhang, Metal-doped carbon nitrides: synthesis, structure and applications, *N. J. Chem.* **45** (27) (2021) 11876–11892.

[31] M. Ma, Z. Huang, D.E. Doronkin, W. Fa, Z. Rao, Y. Zou, R. Wang, Y. Zhong, Y. Cao, R. Zhang, Y. Zhou, Ultrahigh surface density of Co-N2C single-atom-sites for boosting photocatalytic CO<sub>2</sub> reduction to methanol, *Appl. Catal. B: Environ.* **300** (2022).

[32] W.J. Ong, L.L. Tan, S.P. Chai, S.T. Yong, Graphene oxide as a structure-directing agent for the two-dimensional interface engineering of sandwich-like graphene-g-C3N4 hybrid nanostructures with enhanced visible-light photoreduction of CO<sub>2</sub> to methane, *Chem. Commun. (Camb.)* **51** (5) (2015) 858–861.

[33] X.-H. Li, J. Zhang, X. Chen, A. Fischer, A. Thomas, M. Antonietti, X. Wang, condensed graphitic carbon nitride nanorods by nanoconfinement: promotion of crystallinity on photocatalytic conversion, *Chem. Mater.* **23** (19) (2011) 4344–4348.

[34] T. Ma, Q. Shen, B.Z.J. Xue, R. Guan, X. Liu, H. Jia, B. Xu, Facile synthesis of Fe-doped g-C3N4 for enhanced visible-light photocatalytic activity, *Inorg. Chem. Commun.* **107** (2019).

[35] J. Hu, P. Zhang, W. An, L. Liu, Y. Liang, W. Cui, In-situ Fe-doped g-C3N4 heterogeneous catalyst via photocatalysis-Fenton reaction with enriched photocatalytic performance for removal of complex wastewater, *Appl. Catal. B: Environ.* **245** (2019) 130–142.

[36] L. Su, P. Wang, X. Ma, J. Wang, S. Zhan, Regulating local electron density of iron single sites by introducing nitrogen vacancies for efficient photo-fenton process, *Angew. Chem. Int. Ed. Engl.* **60** (39) (2021) 21261–21266.

[37] F. Chen, L.L. Liu, J.H. Wu, X.H. Rui, J.J. Chen, Y. Yu, Single-atom iron anchored tubular g-C(3)N(4) catalysts for ultrafast fenton-like reaction: roles of high-valency iron-oxo species and organic radicals, *Adv. Mater.* **34** (31) (2022) e2202891.

[38] J. Zhang, B. Xin, C. Shan, W. Zhang, D.D. Dionysiou, B. Pan, Roles of oxygen-containing functional groups of O-doped g-C3N4 in catalytic ozonation: quantitative relationship and first-principles investigation, *Appl. Catal. B: Environ.* **292** (2021).

[39] T. Feng, Q. Zeng, S. Lu, M. Yang, S. Tao, Y. Chen, Y. Zhao, B. Yang, Morphological and interfacial engineering of cobalt-based electrocatalysts by carbon dots for enhanced water splitting, *ACS Sustain. Chem. Eng.* **7** (7) (2019) 7047–7057.

[40] M.J. Muñoz-Batista, O. Fontelles-Carceller, A. Kubacka, M. Fernández-García, Effect of exfoliation and surface deposition of MnO<sub>x</sub> species in g-C3N4: Toluene photo-degradation under UV and visible light, *Appl. Catal. B: Environ.* **203** (2017) 663–672.

[41] H. Li, C. Shan, B. Pan, Fe(III)-Doped g-C(3)N(4) mediated peroxymonosulfate activation for selective degradation of phenolic compounds via high-valent Iron-Oxo Species, *Environ. Sci. Technol.* **52** (4) (2018) 2197–2205.

[42] B. Liu, W. Guo, Q. Si, W. Jia, S. Zheng, H. Wang, Q. Zhao, H. Luo, J. Jiang, N. Ren, Atomically dispersed cobalt on carbon nitride for peroxymonosulfate activation: Switchable catalysis enabled by light irradiation, *Chem. Eng. J.* **446** (2022).

[43] X. Zhang, J. Liu, X. Zheng, R. Chen, M. Zhang, Z. Liu, Z. Wang, J. Li, Activation of oxalic acid via dual-pathway over single-atom Fe catalysts: Mechanism and membrane application, *Appl. Catal. B: Environ.* **321** (2023).

[44] H. Cao, J. Wang, J.-H. Kim, Z. Guo, J. Xiao, Y. Yang, J. Chang, Y. Shi, Y. Xie, Different roles of Fe atoms and nanoparticles on g-C3N4 in regulating the reductive activation of ozone under visible light, *Appl. Catal. B: Environ.* **296** (2021).

[45] Y. Wang, X. Li, S. Liu, Y. Liu, T. Kong, H. Zhang, X. Duan, C. Chen, S. Wang, Roles of Catalyst structure and gas surface reaction in the generation of hydroxyl radicals for photocatalytic oxidation, *ACS Catal.* **12** (5) (2022) 2770–2780.

[46] J. Long, Y. Guo, G. Yu, S. Komarneni, Y. Wang, Evaluation of the effect of catalysts on ozone mass transfer and pollutant abatement during laboratory catalytic ozonation experiments: implications for practical water and wastewater treatment, *ACS EST Eng.* **3** (3) (2022) 387–397.

[47] B. Abramovic, V. Despotovic, D. Sojic, N. Fincur, Mechanism of clomazone photocatalytic degradation: hydroxyl radical, electron and hole scavengers, *React. Kinet. Mech. Catal.* **115** (1) (2015) 67–79.

[48] H. Bel Hadjtaief, S. Ben Ameur, P. Da Costa, M. Ben Zina, M. Elena Galvez, Photocatalytic decolorization of cationic and anionic dyes over ZnO nanoparticle immobilized on natural Tunisian clay, *Appl. Clay Sci.* **152** (2018) 148–157.

[49] J. Wang, S. Wang, Effect of inorganic anions on the performance of advanced oxidation processes for degradation of organic contaminants, *Chem. Eng. J.* **411** (2021).

[50] D. Yu, L. Wang, T. Yang, G. Yang, D. Wang, H. Ni, M. Wu, Tuning Lewis acidity of iron-based metal-organic frameworks for enhanced catalytic ozonation, *Chem. Eng. J.* **404** (2021).

[51] R. Oulton, J.P. Haase, S. Kaalberg, C.T. Redmond, M.J. Nalbandian, D.M. Cwiertny, Hydroxyl radical formation during ozonation of multiwalled carbon nanotubes: performance optimization and demonstration of a reactive CNT filter, *Environ. Sci. Technol.* **49** (6) (2015) 3687–3697.

[52] X. Li, D. Wang, S. Zhang, Evaluation of Fe-functionalized 4A zeolite as ozone catalyst for an enhancement of hydroxyl radical pathway in a multiphase reactor, *Ozone.: Sci. Eng.* **41** (2) (2018) 156–165.

[53] Q. Sun, Y. Wang, L. Li, J. Bing, Y. Wang, H. Yan, Mechanism for enhanced degradation of clofibrate acid in aqueous by catalytic ozonation over MnO<sub>x</sub>/SBA-15, *J. Hazard. Mater.* **286** (2015) 276–284.

[54] J.C. Wang, C.X. Cui, Y. Li, L. Liu, Y.P. Zhang, W. Shi, Porous Mn doped g-C(3)N(4) photocatalysts for enhanced synergistic degradation under visible-light illumination, *J. Hazard Mater.* **339** (2017) 43–53.

[55] M. Setka, M. Claros, O. Chmela, S. Vallejos, Photoactivated materials and sensors for NO<sub>2</sub> monitoring, *J. Mater. Chem. C* **9** (47) (2021) 16804–16827.

[56] Q. Sun, L. Li, H. Yan, X. Hong, K.S. Hui, Z. Pan, Influence of the surface hydroxyl groups of MnO<sub>x</sub>/SBA-15 on heterogeneous catalytic ozonation of oxalic acid, *Chem. Eng. J.* **242** (2014) 348–356.

[57] D. Zeng, W.-J. Ong, Y. Chen, S.Y. Tee, C.S. Chua, D.-L. Peng, M.-Y. Han, Co<sub>2</sub>P nanorods as an efficient cocatalyst decorated porous g-C<sub>3</sub>N<sub>4</sub> nanosheets for photocatalytic hydrogen production under visible light irradiation, *Part. Part. Syst. Charact.* **35** (1) (2018).

[58] G. Yu, Y. Wu, H. Cao, Q. Ge, Q. Dai, S. Sun, Y. Xie, Insights into the mechanism of ozone activation and singlet oxygen generation on N-doped defective nanocarbons: a DFT and machine learning study, *Environ. Sci. Technol.* **56** (12) (2022) 7853–7863.

[59] Z. Chen, W. Chen, G. Liao, X. Li, J. Wang, Y. Tang, L. Li, Flexible construct of N vacancies and hydrophobic sites on g-C(3)N(4) by F doping and their contribution to PFOA degradation in photocatalytic ozonation, *J. Hazard. Mater.* **428** (2022) 128222.

[60] J. Xiao, Y. Xie, J. Rabeh, A. Bruckner, H. Cao, Visible-light photocatalytic ozonation using graphitic C(3)N(4) catalysts: a hydroxyl radical manufacturer for wastewater treatment, *Acc. Chem. Res.* **53** (5) (2020) 1024–1033.

[61] G. Yu, Y. Xie, Q. Ge, Q. Dai, J. Xu, H. Cao, Mechanism of ozone adsorption and activation on B-, N-, P-, and Si-doped graphene: a DFT study, *Chem. Eng. J.* **430** (2022).

[62] G. Yu, Y. Wang, H. Cao, H. Zhao, Y. Xie, Reactive oxygen species and catalytic active sites in heterogeneous catalytic ozonation for water purification, *Environ. Sci. Technol.* **54** (10) (2020) 5931–5946.